



RESEARCH ARTICLE

# The Detection of Divalent Iron and Reactive Oxygen Species During Ferroptosis with the Use of a Dual-Reaction Turn-On Fluorescent Probe

Yueqi Wang<sup>1,2</sup> · Changjian Li<sup>3,4</sup> · Jiaming Zhuo<sup>1</sup> · Hui Hui<sup>1,2</sup> · Bing Zhou<sup>3</sup> · Jie Tian<sup>1,2,3,4,5</sup>

Received: 28 June 2022 / Revised: 19 August 2022 / Accepted: 12 September 2022

© The Author(s), under exclusive licence to World Molecular Imaging Society 2022

## Abstract

**Purpose** Ferroptosis, a programmed cell death modality, is an iron-dependent, non-apoptosis pathway that is characterized by the upregulation of divalent iron and reactive oxygen species (ROS) levels. However, the sensitive and rapid detection to track changes in ferroptosis is challenging, partially due to the lack of methods for monitoring the Fe(II) accumulation and ROS generation.

**Procedures** Herein, we reported a dual-reaction fluorescent probe DR-1 with turn-on response, which realized the simultaneous visualizing of Fe(II) and ROS with a single probe. The structure of fluorescence quenching group and turn-on fluorophore constitute a double switch for DR-1, which increases its specificity and stability.

**Results** During ferroptotic cell death, the upregulation of ROS levels led to the cleavage of quenching group of DR-1, and the aggregation of Fe(II) resulting in fluorescence recovery.

**Conclusions** Overall, this study provides a new dual-reaction probe that shows the great potential to explore the mechanism of ferroptosis in vitro and in vivo by fluorescence imaging.

**Key words** Dual-reaction · Fe(II) · Ferroptosis · Fluorescent probes · ROS · Turn-on response

Yueqi Wang and Changjian Li contributed equally to this work.

✉ Hui Hui  
hui.hui@ia.ac.cn

✉ Bing Zhou  
bingzh@buaa.edu.cn

✉ Jie Tian  
tian@ieee.org

<sup>1</sup> CAS Key Laboratory of Molecular Imaging, Beijing Key Laboratory of Molecular Imaging, The State Key Laboratory of Management and Control for Complex Systems, Institute of Automation, Chinese Academy of Sciences, Beijing 100190, China

<sup>2</sup> University of Chinese Academy of Sciences, Beijing 100049, China

<sup>3</sup> School of Engineering Medicine, Beihang University, Beijing 100191, China

<sup>4</sup> Key Laboratory of Big Data-Based Precision Medicine (Beihang University), Ministry of Industry and Information Technology, Beijing 100191, China

<sup>5</sup> Zhuhai Precision Medical Center, Zhuhai People's Hospital, Affiliated With Jinan University, Zhuhai 519000, China

## Introduction

Ferroptosis, a programmed cell death pathway first identified in 2012 by Dixon et al. [1], is an iron-dependent and caspase-independent manner that differs from other types of regulated cell death [1]. Ferroptosis is characterized by the accumulation of lipid peroxides and Fe(II), and the production of lipid peroxides is associated with ROS [1, 2]. Ferroptosis can be induced by a group of chemical compounds such as erastin and RSL3, which inhibit the activity of glutathione peroxidase 4 (GPX4) [3]. As GPX4 is a critical factor for reducing phospholipid hydroperoxide, GPX4 inhibition leads to lipid peroxidation, resulting in the generation of active free radicals that can damage cell function [4, 5]. In addition, SLC7A11, a key component of cystine/glutamate antiporter, its overexpression inhibits ferroptosis induced by ROS [6]. Thus, the dysregulation of ferroptosis is closely associated with various diseases including cancers [7], liver conditions such as liver fibrosis, [8] and neurodegenerative diseases such as dementia [9]. The real-time detection of ferroptosis will help provide necessary information for drug design and disease diagnosis [10]. However, to date, the

most common techniques for detecting ferroptosis, such as western blotting, immunofluorescence, and immunohistochemistry, depend on the level of ferroptosis biomarkers [11, 12]. These conventional methods are typically time-consuming and incapable of rapid, precise, and real-time ferroptosis monitoring in live cells [13]. Thus, it remains necessary to develop probes for the real-time tracking of ferroptosis in living tissues and cells, which can serve as powerful tools for ferroptosis-related preclinical and clinical research.

Since the first report that ferroptosis is iron-dependent, various approaches have been applied to determine the role of iron metabolism in regulating ferroptotic cell death [1]. For example, Gao et al. [14] reported that ferroptotic cell death caused by the extracellular iron carrier protein transferrin was determined by the state of the iron. This finding suggested that the mechanism that controls the iron load of transferrin can also regulate ferroptosis. Thus, ferroptosis occurs due to insufficient cell reduction capacity through Fe(II)-dependent lipid peroxidation [15]. On the other hand, ROS, including  $\text{H}_2\text{O}_2$ ,  $\bullet\text{OH}$ ,  $\bullet\text{O}_2^-$ , and  $\text{HClO}$ , are essential factors in various cellular processes, and an increase in these cellular ROS is also a critical cause of ferroptosis [16–18]. Studies have shown that excess iron imported or released by the autophagy/lysosomal degradation of ferritin or heme catabolism can produce ROS through the Fenton reaction and cause ferroptosis [19, 20]. In contrast, reducing the iron overload using iron-chelating agents impedes ferroptosis induced by erastin [21, 22]. Iron, if present as the form of Fe(II), can trigger the Fenton reaction, even in vivo. [23] These results indicate that simultaneous increases in intracellular Fe(II) and ROS levels are key to the occurrence of ferroptosis. There are many specific and effective methods for the detection of Fe(II) [24] or ROS [25] that have allowed the investigation of their individual roles in ferroptotic cell death [1, 26]. However, there is a lack of effective methods for the real-time simultaneous detection of Fe(II) and ROS during ferroptosis.

Activatable fluorescent probes have been widely used for biomedical imaging because of their improved signal-to-background ratios compared to their “always on” counterparts [27–29]. Fluorescence imaging probes are one of the most effective tools for detecting intracellular Fe(II) and other short-lived species. [24, 30] Most current methods for detecting ferroptosis are based on the use of fluorescent probes to detect a single biomarker of ferroptosis [11, 26]. Although a large number of studies have been conducted to detect ferroptosis, there are few methods that can specifically detect Fe(II) and ROS simultaneously in real time. Moreover, the detections based on antibody are difficult to perform in living cells or in vivo. To address these challenges, Fe(II) or ROS-specific fluorescent small molecules, such as FeRhoNox-1 and 2,7-dichlorofluorescein diacetate (DCFH-DA), have been used to detect ferroptosis [31]. Although

these methods are usually effective, Fe(II) and ROS must be detected separately using two different probes [32]. Owing to the issues associated with the use of different probes, such as uneven site distribution and possible crosstalk in the same cell, this measurement method is not only complicated but also inaccurate. In contrast, a single fluorescent probe which could monitor Fe(II) and ROS simultaneously with high specificity can provide an unprecedented, simple, and accurate method for the study of ferroptosis.

Because of the critical role of Fe(II) in diseased and healthy conditions of living systems, many fluorescent probes for detecting divalent iron have been reported, including chelating fluorescent probes for monitoring “chelated iron groups” and chemical-reaction-based turn-on probes [33]. However, because Fe(II) has the ability to quench fluorescence and the weak binding characteristics of first-row transition metal ions, resulting in the turn-off response and metal selectivity of chelating probes are insufficient [33]. N-oxide-based fluorescent probes are widely used in selective detecting unstable Fe(II) in living cells because of their turn-on response and strong selectivity for redox states and metal ions [34]. Nevertheless, to our knowledge, few current fluorescent probes can simultaneously detect Fe(II) and ROS, which prompted us to design a single molecule probe (DR-1) for using fluorescent imaging to study ferroptosis.

## Materials and Methods

### Reagents and Apparatus

Sodium bicarbonate, ethyl acetate, meta-chloroperoxybenzoic acid (m-CPBA), trifluoroacetic acid (TFA), piperidine, 4-dimethylaminopyridine (DMAP), dicyclohexylcarbodiimide (DCC), dimethyl sulfoxide (DMSO), and thiazolyl blue tetrazolium bromide (MTT) were purchased from Sigma-Aldrich. Erastin, RSL3, ferrostatin-1 (Fer-1), liproxstatin-1 (Lip-1), and deferoxamine mesylate (DFO) were obtained from Med chem Express (Shanghai, China). HepG2, H22, LO2, or LX2 cells were purchased from the American Type Culture Collection (ATCC). The quenching group black hole quencher-2 (BHQ-2) succinimidyl ester was purchased from Biosearch Technologies (USA). All reagents were analytical grade and used directly without further purification. The Wang resin was purchased from Tianjin Nankai Hecheng S&T Co. Ltd (Tianjin, China). RPMI 1640 media, trypsin, and fetal bovine serum (FBS) were purchased from Gibco Invitrogen Co. (New York, NY, USA). Hoechst 33,258 (cat#H3569), 2',7'-dichlorodihydrofluorescein diacetate (H2DCFDA, cat#C10443), mitochondria probe (MitoTracker® Deep Red FM, cat# M22426), and LysoTracker blue (cat# L7525) were purchased from Thermo Fisher Scientific (Loughborough, Leicestershire,

UK). Golgi Tracker Red (cat#C1043) and ER-Tracker Red (cat#C1041) were purchased from Beyotime Biotechnology Co., Ltd, Shanghai, China. Rabbit monoclonal Anti-Glutathione Peroxidase 4 antibody (#ab125066) was purchased from Abcam Trading Co. Ltd (Shanghai, China). SF680-phalloidin (cat#CA1650) was purchased from Solarbio Science & Technology Co., Ltd, Beijing, China. CellMaker Blue CMAC (cat#CS317) was purchased from ZFdows Bio Co., Ltd, Nanjing, China.

Ultrapure water (over 18 MΩ·cm) from a Milli-Q reference system (Merck Millipore, MA, USA) was employed throughout. The absorption spectra were characterized by a Shimadzu UV-2550 spectrophotometer. The fluorescence emission spectra were obtained by an F-7000 fluorescence spectrofluorometer (Hitachi, Japan). Electrospray ionization mass spectrometry (ESI-MS) was performed at Thermo Finnigan LCQ Deca XP MAX mass spectrometer. Cytotoxicity of DR-1 was evaluated by MTT assay in a previous study [35] on a SpectraMax i3 microplate reader (Molecular Devices, USA). Confocal fluorescence images were obtained on LSM710 confocal laser scanning microscope (Zeiss, Germany) and FV 1200-IX83 confocal laser scanning microscope (Olympus, Japan). Liquid chromatography with tandem mass spectrometry (LC-MS/MS 8050, Shimadzu Corporation) was used for the quantification of 4-aminobutyric acid (GABA) in biological samples.

### Synthesis and Characterization of DR-1

DR-1 was synthesized according to the following methods. As shown in Figure S1, compound 1, which is a rhodamine B-based turn-on fluorescent probe used for ferrous ion detection, was synthesized according to a previous literature [30]. The crude product of compound 1 was purified by HPLC and then verified by mass spectrometry (shown in Figure S2). Then, ROS-responsive peptide modified with a fluorescence quenching group, BHQ-2 succinimidyl ester at the lysine residue of the peptide, was prepared by a strategy that used solid-phase peptide synthesis through an Fmoc-amino protection strategy. The sequence of ROS-responsive peptide was CPPPPPK. After the N-terminal Fmoc group was removed by 20% piperidine in DMF, compound 1 was reacted with the amino group at the end of the peptide. Then, DR-1, as the final product was obtained after peptide cleavage from Wang resin, and the crude product was purified by HPLC and then verified by mass spectrometry.  $\text{FeCl}_2 + \text{H}_2\text{O}_2$ :  $\text{H}_2\text{O}_2$  solution was slowly added to the tube containing DR-1 and  $\text{FeCl}_2$ .

### Cell Culture

HepG2 cells were cultured in DMEM media supplemented with 10% fetal bovine serum, 100 units/mL penicillin, and

100 µg/mL streptomycin at 37 °C in a humidified atmosphere of 95% air and 5%  $\text{CO}_2$ . After growing to 70% confluence, the cells were treated with trypsin, and then seeded on glass bottom dishes for 24 h for further experiments.

### In Vitro Fluorescence Imaging

HepG2 cells were treated with 10 µM erastin or 2 µM RSL3 for the appropriate time to induce ferroptosis [3]. After that, the culture media were removed and the cells were washed with serum-free media and then incubated with 10 µM DR-1 for 1 h. To inhibit ferroptosis, the cells were incubated with 10 µM erastin or 2 µM RSL3 in the presence of 100 µM DFO, 5 µM Fer-1, or 5 µM Lip-1 [1, 21]. Fluorescence imaging was performed with the confocal laser scanning microscope.

### Animals and Establishment Mouse Tumor Models

Balb/c female nude mice (6 weeks of age) were purchased from Vital River Laboratory Animal Technology Co. Ltd., Beijing, China. All the experimental procedures involving animals were approved by the Institutional Animal Care and Use Committee of the Institute of Automation, Chinese Academy of Sciences. HepG2 cells ( $1 \times 10^6$ ) were suspended in 100 µl PBS and injected into the nude mice subcutaneously. The tumors were allowed to grow to about 200 mm<sup>3</sup> before the experiment.

### In Vivo and Ex Vivo Fluorescence Imaging

HepG2-bearing nude mice were randomly divided into two groups, and ferroptosis was induced by injection of erastin (10 mg/kg) every 2 days for 1 week; mice without any treatment were used as a negative control. Then, DR-1 (10 mg/kg) was injected into the mice; the fluorescence change of DR-1 was monitored after injection of 1 h using IVIS spectrum imaging system (PE, Waltham, MA, USA). The tumors were excised, fixed in 4% PFA, and transferred to a 30% sucrose aqueous solution for 12 h. Coronal frozen Sects. (10 µm in thickness) of tumors were cut using a cryotome (Microm, Germany). Finally, the sections were observed by a Nikon TiE microscope (Nikon, Tokyo, Japan).

### Immunohistochemistry

Paraffin-embedded tissue sections from mice were baked at 60 °C for 1 h. Slides were deparaffinized with xylene, rehydrated in ethanol, and rinsed in distilled water. The tumor sections were incubated with 3%  $\text{H}_2\text{O}_2$  in methanol at room temperature for 20 min and antigen repair at 95°C for 5 min. After washing thrice in PBS, the sections were blocked in 10% goat serum for 30 min to prevent non-specific binding,

followed by incubation with the primary antibody (GPX4, Abcam, #ab125066 or SLC7A11, Abcam, #ab37185). Next, the sections were washed and incubated with HRP-labeled secondary antibody for 30 min. The nuclei were labeled by hematoxylin and the substrate DAB was added for 10 min. The images were captured using a Nikon TiE microscope (Nikon, Tokyo, Japan).

## Statistical Analysis

Statistical analysis was performed using GraphPad Prism V5.0 (GraphPad Software, Inc., San Diego, CA, USA). All data are expressed as the mean  $\pm$  standard deviation (SD). For comparisons between two groups, statistical significance was analyzed with Student's *t*-tests ( $P < 0.05$  was considered statistically significant). For comparisons of three or more groups, statistical significance was analyzed with one-way ANOVA ( $*P < 0.05$  considered significant).

## Results and Discussion

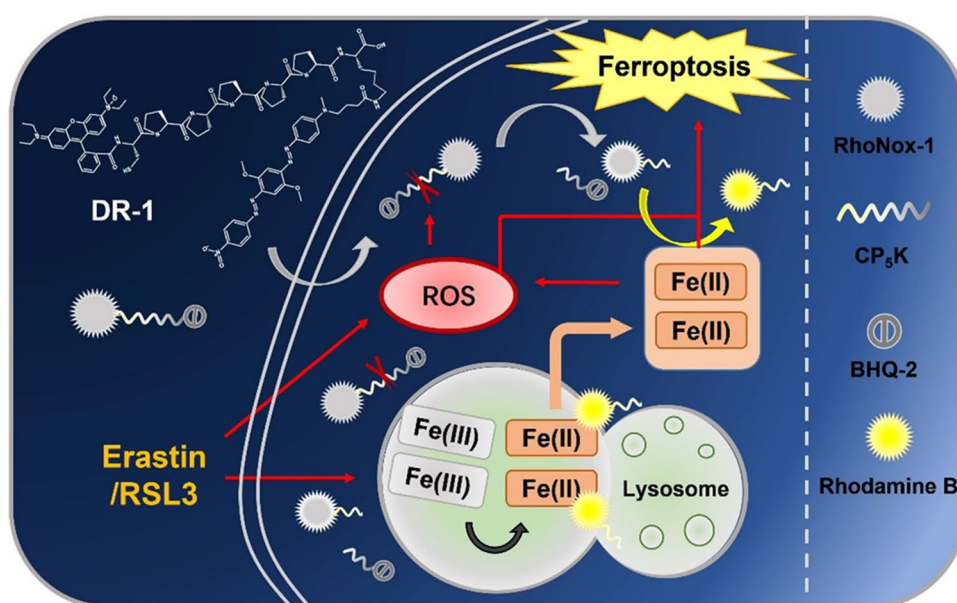
### Dual-Reaction Turn-On Mechanism of DR-1 in Detection of Fe(II) and ROS

To explore the mechanism of ferroptosis in living cells, it is necessary to monitor Fe(II) accumulation and ROS generation simultaneously with a single dye. Therefore, an ideal probe for quantitative Fe(II) and ROS detection will only induce fluorescence changes when both factors are present. For this reason, we designed a turn-on probe with a dual response to Fe(II) and ROS. An Fe(II)-specific turn-on fluorophore [30] was used to connect an ROS-degradable

peptide chain[36] and a fluorescence quenching group to achieve a double response and double switch for the detection of ferroptosis (Scheme 1). Common detection methods for Fe(II) include traditional and chemical-reaction-based fluorescent probes. Chemical reaction-based fluorescent probes take advantage of the unique chemical reactivity of Fe(II) and feature a highly selective turn-on response following the reaction with the target molecule. This selective turn-on detection mechanism has been used to explore the biological and pathological roles of Fe(II) in determining the redox state of cells. RhoNox-1 achieves a high selective Fe(II) detection through tertiary amine N-oxide deoxygenation mediated by Fe(II) [34]. Therefore, we based our probe DR-1 on RhoNox-1, a fluorophore with a rhodamine B scaffold with the conversion of one amino group to tertiary amine N-oxide.

To achieve a simultaneous response to ROS, we also incorporated an ROS-degradable polypeptide into DR-1. This peptide containing oligoproline was aimed to respond to a series of chemical species of ROS. The specific mechanism of its reaction with ROS oxidation is closely related to proline oxidation and peptide bond breaking [37, 38]. The high levels of ROS associated with ferroptosis in living cells will degrade the peptide chain, thereby releasing the quenching group and turning on the first switch. At this time, the probe will still display negligible fluorescence because the N-oxide group reduces electron donation from the nitrogen atom and prevents its lone pair from participating in the conjugated xanthene system, which causes a hypsochromic shift in the absorption band and a reduction in fluorescence. However, the N-oxide unit of DR-1 was readily decomposed by the reaction with Fe(II) and recovered the parent fluorophore moiety rhodamine B, leading to the turning on of

**Scheme 1** We design a turn-on fluorescent probe for the simultaneous detection of Fe(II) and ROS; an N-oxide-based fluorophore and an ROS-degradable peptide chain were introduced onto a rhodamine B scaffold and connected to a fluorescence quenching group. In the DR-1 structure, ROS can degrade the amino acid sequence in the polypeptide chain, resulting in cleavage of the quenching group. Due to the reaction of the N-oxide unit of DR-1 with Fe(II), the probe recovers fluorescence from rhodamine B.





the second fluorogenic switch. In summary, the transformation of DR-1 into its products without quenching group in the presence of ROS causes a fluorescent turn-on response by Fe(II), which allows the probe to detect Fe(II) and ROS simultaneously during ferroptosis in living cells (Fig. 1a). DR-1 exhibits absorption ( $\lambda_{\text{max}} = 492 \text{ nm}$ ) and fluorescence emission ( $\lambda_{\text{em,max}} = 575 \text{ nm}$ ) in the visible region.

## Preparation and Characterization of DR-1

The probe was synthesized according to the synthetic route described in Figure S1. A fluorophore containing a nitro group was used to connect the peptide segment with a repeated amino acid sequence through an amidation reaction to obtain a double response to ROS and Fe(II). We introduced BHQ-2 as the quenching group, which is known to have a strong absorption range of 520–600 nm and good quenching of fluorophores emitting fluorescence in this range [39]. Subsequently, BHQ-2 was connected to obtain the final turn-on fluorescent probe. The final product was

confirmed to be DR-1 by high-resolution mass spectrum and high-performance liquid chromatography (Figures S2 and S3). The oxidation of proline residues of proteins can lead to peptide bond cleavage by a mechanism that involves oxidation of the proline residues to the 2-pyrrolidone derivative. Furthermore, the acid hydrolysis of 2-pyrrolidone yields GABA [37, 38]. As shown in Figure S3d, GABA was detected in the products, which verified the degradation of pro-containing peptides mediated by hydroxyl radicals.

RhoNox-1 (compound 1 in Figure S1) was used to evaluate the fluorescence response to Fe(II) in the buffer (50 mM 4-(2-hydroxyethyl)-1-piperazineethanesulfonic acid (HEPES), pH 7.4). As expected, RhoNox-1, which does not contain the quenching group, showed an absorption and emission maximum at 492/575 nm (Fig. 1b). When treated with Fe(II), RhoNox-1 showed increased emission at 575 nm. At a concentration of 10  $\mu\text{M}$ , RhoNox-1 was able to sense 0.25–20  $\mu\text{M}$  Fe(II) in the phosphate-buffered saline (PBS) buffer with a dose-dependent response (Figure S4a). RhoNox-1 was confirmed to exhibit a fluorescence response

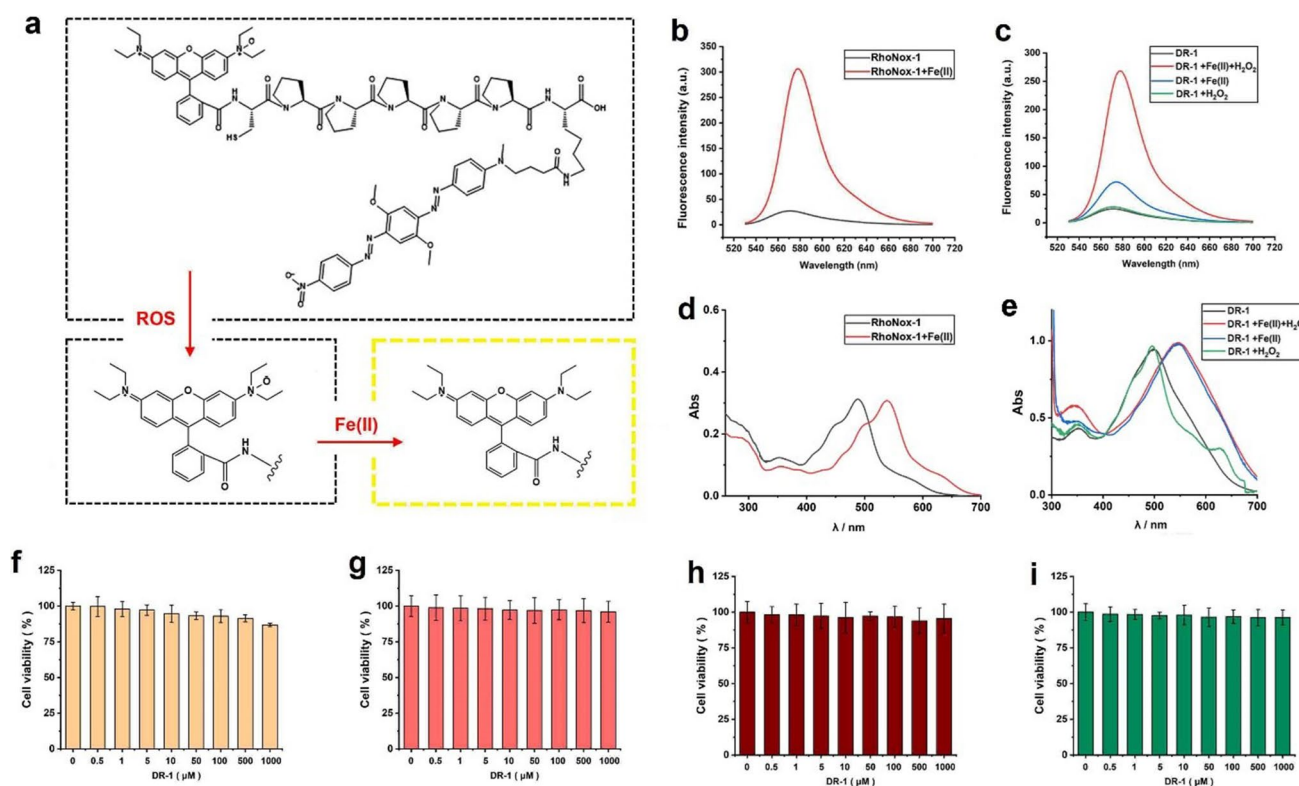


**Fig. 1** Dual-reaction turn-on mechanism of DR-1 in the detection of Fe(II) and ROS. **a** The response mechanism and characterization of DR-1. **b** The fluorescence spectra of RhoNox-1 (10  $\mu\text{M}$ ) in the absence and presence of 50  $\mu\text{M}$  FeCl<sub>2</sub>.  $\lambda_{\text{ex}} = 492 \text{ nm}$ ,  $\lambda_{\text{em}} = 575 \text{ nm}$ . **c** The fluorescence spectra of DR-1 (10  $\mu\text{M}$ ) in pH 7.4 phosphate buffer containing different reaction systems: 50  $\mu\text{M}$  FeCl<sub>2</sub>, 50  $\mu\text{M}$  H<sub>2</sub>O<sub>2</sub>, and 50  $\mu\text{M}$  FeCl<sub>2</sub> + 50  $\mu\text{M}$  H<sub>2</sub>O<sub>2</sub>. **d** The UV-vis spectra of RhoNox-1 (10  $\mu\text{M}$ ) in the absence and presence of 50  $\mu\text{M}$  FeCl<sub>2</sub>. **e** The UV-vis

spectra of DR-1 (10  $\mu\text{M}$ ) in pH 7.4 phosphate buffer containing different reaction systems: 50  $\mu\text{M}$  FeCl<sub>2</sub>, 50  $\mu\text{M}$  H<sub>2</sub>O<sub>2</sub>, and 50  $\mu\text{M}$  FeCl<sub>2</sub> + 50  $\mu\text{M}$  H<sub>2</sub>O<sub>2</sub>. **f–i** The cell viability was determined by the standard MTT method, and the viability in the absence of DR-1 was defined as 100%. The results are presented as mean  $\pm$  standard deviation ( $n = 5$ ). The viability of HepG2, H22, LO2, or LX2 cells incubated with different concentrations of DR-1 for 12 h.

to Fe(II), with the fluorescence increasing significantly with an increase in the Fe(II) concentration. Owing to the presence of both the fluorescence turn-on response and the quenching group, DR-1 did not emit strong fluorescence in the physiological buffer or normal living cells. Therefore, we studied the response characteristics of DR-1 to metal cations in the presence of ROS.

### Simultaneous Response to Fe(II) and ROS in *Ex Vivo*

Under the optimized condition (reacting for 1 h at physiological pH 7.4, Figure S4b), the fluorescence response of DR-1 to different amounts of treatment is shown in the fluorescence spectra. As illustrated in Fig. 1c, compared to the treatment of Fe(II) or H<sub>2</sub>O<sub>2</sub> alone, the fluorescence of DR-1 increased when exposed to both Fe(II) and H<sub>2</sub>O<sub>2</sub> in 50 mM HEPES buffer (pH 7.4). Next, we evaluated the selectivity of DR-1 to Fe(II) in the presence of ROS by comparison with the response to alkaline earth metals, alkali metals, and biologically relevant transition metals (Figure S5a). DR-1 exhibited a highly metal-specific response to Fe(II) in the presence of H<sub>2</sub>O<sub>2</sub>. Furthermore, DR-1 showed high selectivity for ROS with the treatment of Fe(II); no significant fluorescence enhancement was detected upon the addition of inorganic salts and biologically active substances. For example, with the presence of amino acids, glucose, or glutathione, DR-1 cannot achieve Fe(II) detection (Figure S5b). In addition, DR-1 showed an absorption band at around 492 nm in phosphate buffer (pH 7.4) containing H<sub>2</sub>O<sub>2</sub>. However, FeCl<sub>2</sub> or FeCl<sub>2</sub> + H<sub>2</sub>O<sub>2</sub> caused the absorption peak of DR-1 to shift to 575 nm (Fig. 1d, e), which can be attributed to the conversion

of DR-1 to rhodamine B. These observations indicate that DR-1 has sufficient *in vitro* and *ex vivo* selectivity (Figure S6) which can be used in biological systems for detecting Fe(II) and ROS simultaneously. As shown in Figure S7, the fluorescence of DR-1 was not affected by temperature variations. Therefore, the effect of temperature and pH did not interfere with the fluorescence of DR-1, which is essential for monitoring Fe(II) and ROS accurately.

### Monitoring Fe(II) and ROS Simultaneously *In Vitro*

A standard MTT assay showed relatively high cell viability even at a DR-1 concentration of 100  $\mu$ M and incubation with HepG2, H22, LO2, or LX2 cells for 12 h (Fig. 1f–i). These results confirmed that DR-1 has good biocompatibility, which predicts that this is a safe probe to use in detecting dynamic processes of living cells.

The liver cancer HepG2 cells were selected to establish a ferroptosis cell model. Erastin and RSL3 are ferroptosis inducers [1, 3] that inhibit the uptake of intracellular cystine, which results in the subsequent accumulation of Fe(II) and ROS. We further verified the feasibility of using DR-1 to detect ferroptosis by incubating HepG2 cells with PBS, FeCl<sub>2</sub>, H<sub>2</sub>O<sub>2</sub>, erastin, or RSL3 for 12 h, and then stained the cells with DR-1 for 60 min. The imaging performance of DR-1 for ferroptotic cell death was investigated using confocal fluorescence microscopy. RSL3 induced ferroptosis by covalently inhibiting GPX4 [3], and similar imaging results were also observed in HepG2 cells treated with erastin. As depicted in Fig. 2a, b, and c, compared with the control group, the fluorescence intensity of the FeCl<sub>2</sub> or

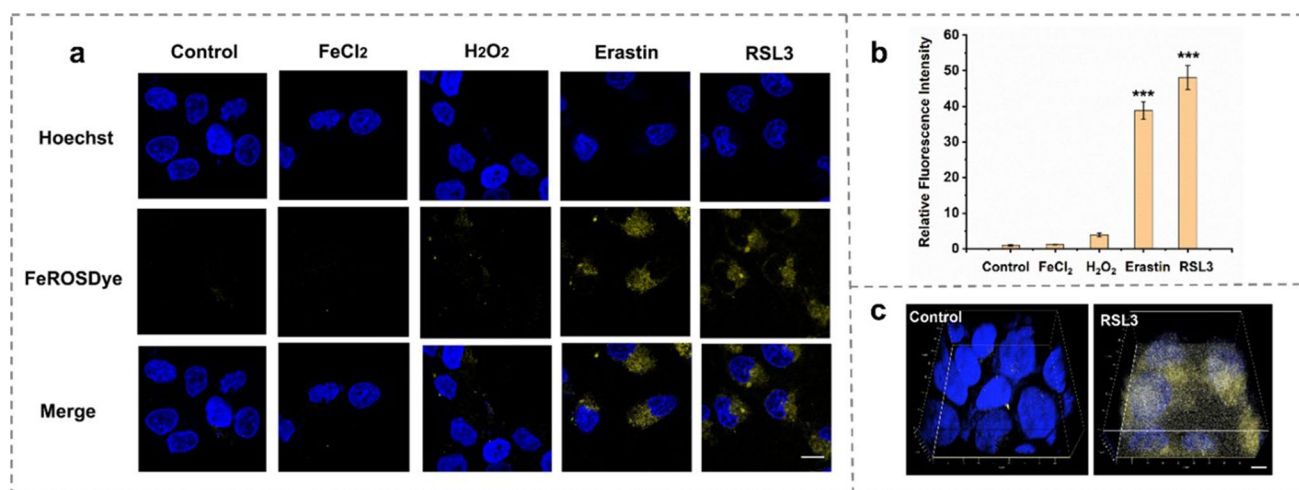


**Fig. 2** Monitoring Fe(II) and ROS simultaneously *in vitro*. **a** Cells were treated with dimethyl sulfoxide (control group), FeCl<sub>2</sub>, H<sub>2</sub>O<sub>2</sub>, erastin, or RSL3. Cells were stained with DR-1 (20  $\mu$ M,  $\lambda_{\text{ex}}$ =492 nm,  $\lambda_{\text{em}}$ =575 nm) and Hoechst (blue,  $\lambda_{\text{ex}}$ =405 nm,  $\lambda_{\text{em}}$ =430–470 nm) before imaging. DR-1 is pseudocolored in yellow. Scale bar: 20  $\mu$ m. **b** Relative fluorescence intensity of the fluorescence images in **a**. The pixel intensity from the image (control

group) is defined as 1.0.  $\lambda_{\text{ex}}$ =492 nm,  $\lambda_{\text{em}}$ =575 nm. The results are presented as mean  $\pm$  standard deviation ( $n$ =3). Significant differences (\*\*\*)  $p$ <0.001 vs control group) are performed by Student's *t*-test. **c** 3D confocal images of HepG2 cells incubated with DR-1 (20  $\mu$ M,  $\lambda_{\text{ex}}$ =492 nm,  $\lambda_{\text{em}}$ =575 nm) and Hoechst (10  $\mu$ M,  $\lambda_{\text{ex}}$ =405 nm,  $\lambda_{\text{em}}$ =430–470 nm) in serum-free medium with or without RSL3. Scale bar: 5  $\mu$ m.

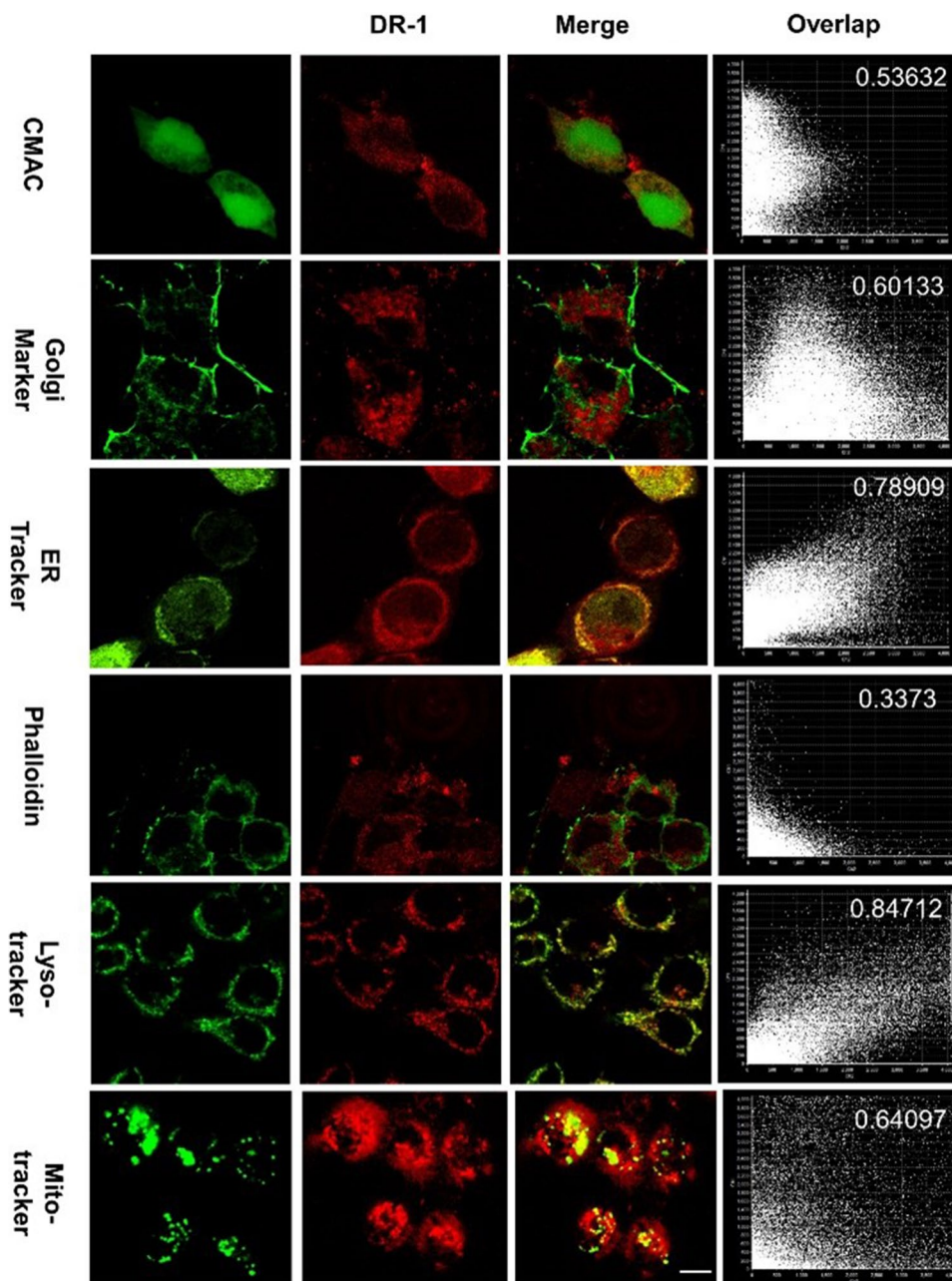
H<sub>2</sub>O<sub>2</sub> treatment groups showed no significant change, whereas the fluorescence intensity of the erastin or RSL3 treatment groups increased significantly (Video S1 and S2 shown in the supporting information). In addition, erastin or RSL3 itself had no effect on the fluorescence of DR-1 (Figure S8, S9). These results indicate that DR-1 can image ferroptotic changes during cell damage.

### Intracellular Distribution of the Released Fluorophore from DR-1 During Ferroptosis

HepG2 cells were stained with DR-1 and CMAC (cytoplasmic blue fluorescent dye, cytoplasmic matrix probe) [40],

Golgi Tracker (Golgi probe), phalloidin (cytoskeleton probe), LysoTracker Blue (lysosomal probe), MitoTracker Deep Red FM (mitochondrial probe) or ER-Tracker Red (endoplasmic reticulum probe). As shown in Fig. 3, the fluorescence signal of the released rhodamine B-containing products was overlapped with that of LysoTracker Blue ( $\lambda_{em} = 575$  nm). Moreover, a high Pearson's correlation coefficient (0.84712) and overlap coefficient (0.831) were seen in the intensity correlation plot. By comparison, the cleaved fluorescent compound did not remarkably stain the cytoplasmic membrane or cytoskeleton. These results indicate that the released fluorophore is likely to accumulate selectively in lysosomes, Golgi, ER, and mitochondria. Consistently, it was reported that the

**Fig. 3** Intracellular distribution of the released fluorophore from DR-1 during ferroptosis. Representative confocal fluorescence images of colocalization of DR-1 in HepG2 cells. Erastin-treated cells were incubated with 20  $\mu$ M DR-1 and CellMaker Blue CMAC ( $\lambda_{ex} = 353$  nm,  $\lambda_{em} = 466$  nm), Golgi Marker ( $\lambda_{ex} = 589$  nm,  $\lambda_{em} = 617$  nm), ER-Tracker ( $\lambda_{ex} = 587$  nm,  $\lambda_{em} = 615$  nm), Phalloidin ( $\lambda_{ex} = 681$  nm,  $\lambda_{em} = 698$  nm), LysoTracker ( $\lambda_{ex} = 373$  nm,  $\lambda_{em} = 422$  nm), or MitoTracker ( $\lambda_{ex} = 644$  nm,  $\lambda_{em} = 665$  nm). Note: the cells were fixed with paraformaldehyde and permeabilized with Triton X-100 before staining with Phalloidin. Probes are indicated or pseudocolored in representative confocal images. The intensity correlation plot of DR-1 and other probes are shown in the last column. Scale bar: 10  $\mu$ m.





divalent iron involved in ferroptosis is mainly produced in lysosomes, which is the main site where trivalent iron is converted into divalent iron by enzymes [41]. Moreover, the dysfunction of lysosomes leads to iron accumulation and ROS production, which promotes lipid peroxidation and leads to ferroptosis [31, 42]. However, compared with other pH regions, DR-1 shows relatively high fluorescence in the region of pH=4–6 (Figure S10). Therefore, the acid environment of lysosomes may affect the fluorescence response of DR-1. Previous imaging studies have shown that intracellular labile Fe(II) levels in lysosomes and endoplasmic reticulum increase during erastin-induced cell death. In addition, the increase of fluorescence signal in mitochondria is due to the shrinkage of mitochondria rather than the increase of the Fe(II) level [43]. Moreover, Golgi apparatus may be a key organelle which holds a large amount of labile Fe(II) [44]. Therefore, the intracellular distribution of the released rhodamine B-containing products showed that Fe(II) may accumulate in lysosomes, Golgi, and ER under the action of ROS during ferroptosis.

## Real-Time Imaging of DR-1 in Ferroptosis Cell Model

Further assays were performed to prove that DR-1 can be applied to detect Fe(II) and ROS during ferroptosis in real time. HepG2 cells were treated with erastin (0–12 h) and then stained with DR-1. Confocal images indicated that the fluorescence of DR-1 increased with increasing erastin treatment time. As depicted in Fig. 4a, the fluorescence of DR-1 increased slightly within 4 h of erastin treatment, and the fluorescence in the cells became stronger with increasing treatment time. Some cells were observed to contract at 12 h, indicating cell damage or death. As is seen from Fig. 4b, cells treated with erastin for 6 h, 8 h, or 12 h produced 2.0-, 2.4-, or 3.7-fold fluorescence enhancement, respectively, at  $\lambda_{em}=575$  nm as compared to the HepG2 cells incubated with erastin for 4 h. Furthermore, a linear relationship between fluorescence intensity and erastin concentration can be observed (Figure S11), indicating that DR-1 can detect mild ferroptosis in HepG2 cells caused by erastin as low as 1  $\mu$ M.

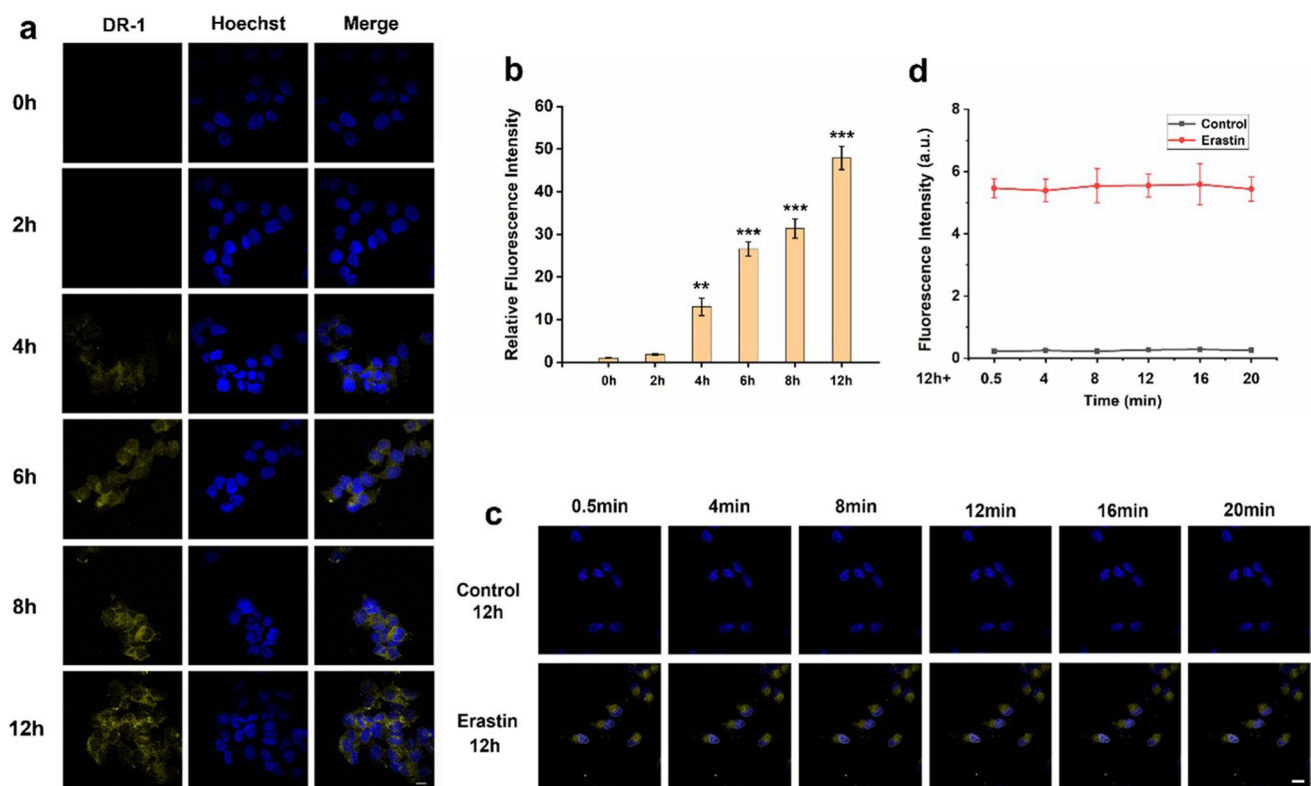


**Fig. 4** Real-time imaging of DR-1 in ferroptosis cell model. **a** Representative confocal fluorescence images of HepG2 cells loaded with DR-1. HepG2 cells were treated with erastin (10  $\mu$ M) for 0–12 h then stained with DR-1 (20  $\mu$ M,  $\lambda_{ex}=492$  nm,  $\lambda_{em}=575$  nm) and Hoechst (blue). DR-1 is pseudocolored in yellow. Scale bar: 20  $\mu$ m. **b** Relative fluorescence intensity of the fluorescence images in **a**. The pixel intensity from the image (2 h group) is defined as 1.0.  $\lambda_{ex}=492$  nm,  $\lambda_{em}=575$  nm. The results are presented as mean  $\pm$  standard deviation ( $n=3$ ). Significant differences (\*\* $p<0.01$ ; \*\*\* $p<0.001$  vs

2 h group) are performed by Student's *t*-test. **c** Representative real-time confocal fluorescence images of living cells loaded with DR-1. HepG2 cells were stained with DR-1 (20  $\mu$ M,  $\lambda_{ex}=492$  nm,  $\lambda_{em}=575$  nm) and Hoechst (blue) in serum-free medium with or without erastin. DR-1 is pseudocolored in yellow. Scale bar: 20  $\mu$ m. **d** The fluorescence intensity of the fluorescence images in **c**.  $\lambda_{ex}=492$  nm,  $\lambda_{em}=575$  nm. The results are presented as mean  $\pm$  standard deviation ( $n=3$ ).



These results reveal that the fluorescence of DR-1 can be used to detect ferroptotic changes in living cells in real time.

To test the stability of DR-1 for imaging, the cells were treated with erastin for 12 h, and then real-time imaging of living cells was evaluated in a serum-free medium supplemented with DR-1. The time-lapse video obtained from continuous confocal imaging over 20 min showed that continuous irradiation did not lead to rapid fluorescence quenching (video S3 shown in the supporting information). The pictures in Fig. 4c were snapshotted from the video of the measurement process. Thus, DR-1 has good photostability (Fig. 4d) and is suitable for long-term live cell imaging to detect real-time dynamic changes associated with ferroptosis in the cell.

### In Vitro Imaging of DR-1 with the Inhibition of Ferroptosis

Deferoxamine (DFO) [1], ferrostatin-1 (Fer-1), and liproxstatin-1 (Lip-1) [21] were used as ferroptosis inhibitors.

HepG2 cells pretreated with DFO (100  $\mu$ M), Fer-1 (5  $\mu$ M), or Lip-1 (5  $\mu$ M) were incubated with erastin, and then DR-1 staining was applied to detect ferroptosis. Additionally, we used DR-1 staining to detect caspase-dependent apoptosis induced by treating HepG2 cells with 10  $\mu$ M carbonyl cyanide 3-chlorophenylhydrazone (CCCP) [45]. As shown in Figs. 5a and S12, treatment with erastin (10  $\mu$ M) for several hours induced cell injury. However, this process was effectively inhibited by the addition of DFO, which is an iron chelator, indicating that this type of cell death is iron-dependent. The confocal images showed that DR-1 fluorescence was significantly enhanced in cells treated with erastin alone, whereas almost no DR-1 fluorescence was observed in cells pretreated with Fer-1 or Lip-1. These results indicated that DR-1 can detect intracellular ferroptosis, and Fer-1 or Lip-1 effectively inhibited the fluorescence signals. Notably, compared with the control group, no significant increase in fluorescence was observed in the apoptosis group. However, the treatment of DFO resulted in a fluorescence reduction

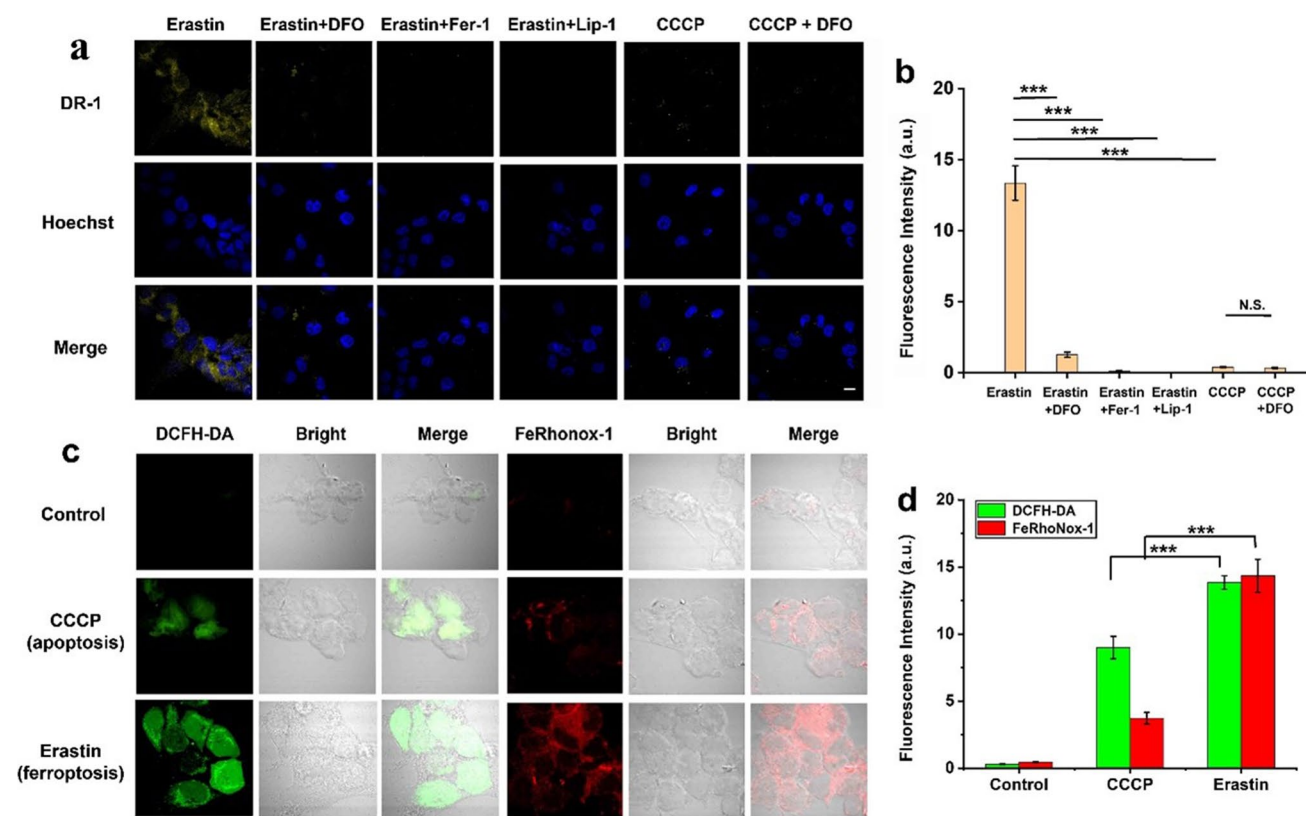


**Fig. 5** In vitro imaging of DR-1 with the inhibition of ferroptosis. **a** Representative confocal fluorescence images of HepG2 cells loaded with DR-1. HepG2 cells were treated with DFO (100  $\mu$ M), Fer-1 (5  $\mu$ M), or Lip-1 (5  $\mu$ M) in the presence of 10  $\mu$ M erastin for 12 h before being stained with DR-1 (20  $\mu$ M,  $\lambda_{ex}$ =492 nm,  $\lambda_{em}$ =575 nm) and Hoechst (blue). DR-1 is pseudocolored in yellow. Scale bar: 20  $\mu$ m. **b** Relative fluorescence intensity of the fluorescence images in **a**. The results are presented as mean  $\pm$  standard deviation ( $n$ =3,

respectively; one-way ANOVA; N.S.: no significant difference; \* $P$ <0.05; \*\* $P$ <0.01; \*\*\* $P$ <0.001; \*\*\*\* $P$ <0.0001). **c** The confocal images of HepG2 cells under different conditions incubated with DCFH-DA (5  $\mu$ M,  $\lambda_{ex}$ =504 nm,  $\lambda_{em}$ =529 nm) or FeRhoNox-1 (5  $\mu$ M,  $\lambda_{ex}$ =492 nm,  $\lambda_{em}$ =575 nm). Scale bar: 20  $\mu$ m. **d** The results are presented as mean  $\pm$  standard deviation ( $n$ =3). Significant differences (\*\*\* $p$ <0.001 vs apoptosis group) are performed by Student's  $t$ -test.

of approximately 90% in the ferroptosis group (Fig. 5b). In addition, the levels of Fe(II) and ROS of HepG2 cells in the apoptosis group induced by CCCP were significantly lower than those in the ferroptosis group, as detected by FeRhoNox-1 (Fe(II) probe) and DCFH-DA (ROS probe) staining[46] (Fig. 5c and d). These findings indicate that ferroptosis is accompanied by coexisting Fe(II) and ROS.

### Identification of Fe(II) and ROS by DR-1 *In Vivo*

In addition to the ferroptosis detection by DR-1 in living cells, we also used the probe for *in vivo* imaging in BALB/c nude mice and tumor-bearing nude mice. First, we added DR-1 to Eppendorf (EP) tubes containing normal saline, FeCl<sub>2</sub>, H<sub>2</sub>O<sub>2</sub>, or FeCl<sub>2</sub> + H<sub>2</sub>O<sub>2</sub> solutions, and images were obtained using an *in vivo* imaging system (IVIS Spectrum, USA). The EP tube with FeCl<sub>2</sub> + H<sub>2</sub>O<sub>2</sub> solution exhibited bright fluorescence as shown in Fig. 6a. We embedded PBS, FeCl<sub>2</sub>, H<sub>2</sub>O<sub>2</sub>, and FeCl<sub>2</sub> + H<sub>2</sub>O<sub>2</sub> in Matrigel solutions and these mixtures were intramuscular injected slowly into the

legs of nude mice. After the intramuscular of DR-1, intense fluorescence ( $\lambda_{em}=575$  nm) was only observed from the FeCl<sub>2</sub> + H<sub>2</sub>O<sub>2</sub> implants, which reached a maximum value after 1.5 h (Figs. 6b, c and S13). The fluorescence from all the other implants was similar to the background value. We also applied DR-1 for the *in vivo* imaging with ferroptosis-induced HepG2 cells in tumor-bearing mice. Ferroptosis was induced by intratumoral injection of erastin every 2 days for 1 week, and then DR-1 was intratumoral injected for *in vivo* fluorescence imaging. Compared with the mice without erastin treatment, the erastin-treated mice showed enhanced fluorescence ( $\lambda_{em}=575$  nm), indicating the accumulation of Fe(II) and ROS during ferroptosis (Figs. 6d and S14). Subsequently, the tumors were collected, sectioned, and imaged using an automatic digital slide scanner. As shown in Fig. 6e and f, the tumor sections with cellular ferroptosis emitted enhanced fluorescence at  $\lambda_{em}=575$  nm. In comparison, the tumor sections without erastin treatment exhibited faint fluorescence, which was consistent with the *in vivo* optical imaging results. The immunohistochemical results of the tumor sections showed

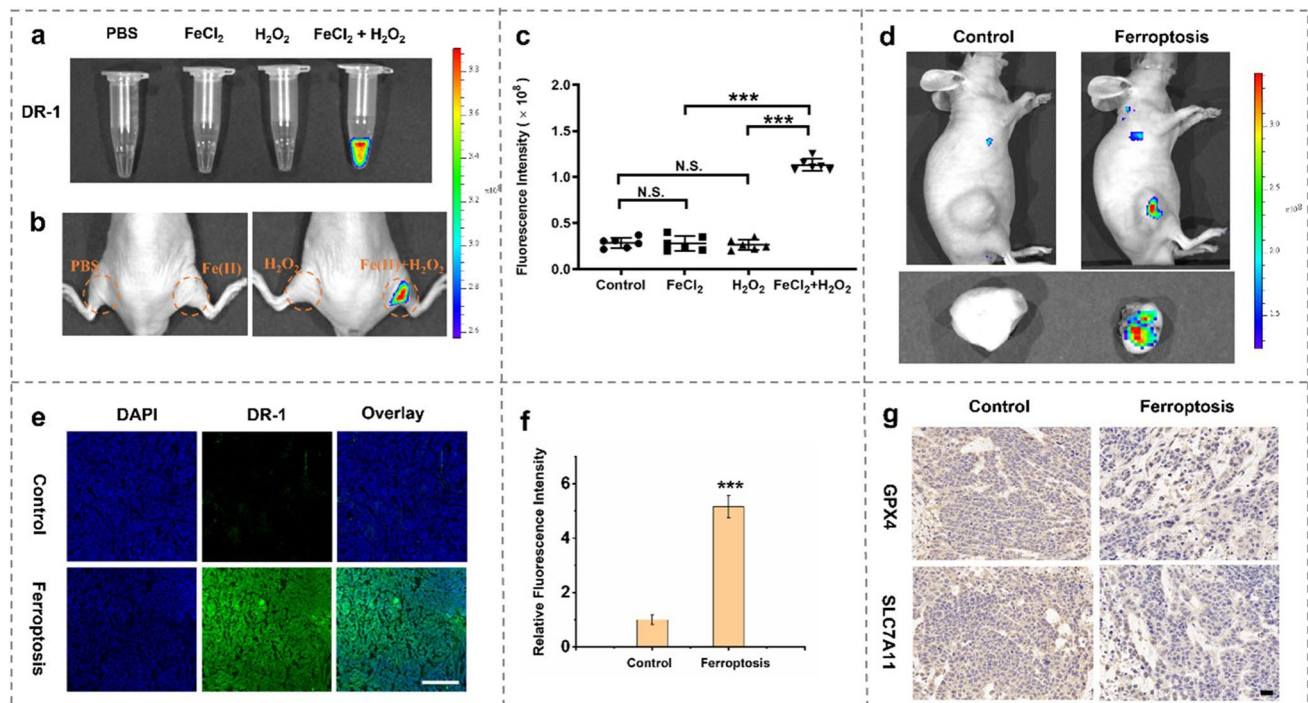


**Fig. 6** Identification of Fe(II) and ROS by DR-1 *in vivo*. **a** Fluorescence molecular imaging of DR-1 (10  $\mu$ M) in different reaction systems. **b** In vivo verification of DR-1. PBS, Fe(II), H<sub>2</sub>O<sub>2</sub>, or Fe(II) + H<sub>2</sub>O<sub>2</sub> were embedded in Matrigel, and subcutaneous implants were established in nude mice. Fluorescence molecular imaging was initiated after injection of DR-1 (10 mg/kg).  $\lambda_{ex}=492$  nm,  $\lambda_{em}=575$  nm. **c** The fluorescence intensity of the fluorescence images in **b**. The results are presented as mean  $\pm$  standard deviation ( $n=6$ , respectively; one-way ANOVA; N.S.: no significant difference; \* $P<0.05$ ; \*\* $P<0.01$ ; \*\*\* $P<0.001$ ; \*\*\*\* $P<0.0001$ ). **d** Top: whole-body images were acquired after injection of DR-1 (10 mg/kg)

with HepG2 cells in tumor-bearing mice; bottom: ex vivo fluorescent images of tumors from mice.  $\lambda_{ex}=492$  nm,  $\lambda_{em}=575$  nm. **e** Fluorescence images of tumor frozen sections. DR-1 is pseudocolored in green. The sections were visualized using DAPI (blue) for the nuclei. Scale bar: 200  $\mu$ m. **f** Relative fluorescence intensity of DR-1 for both control and ferroptosis samples. The pixel intensity from control group is defined as 1.0. The results are presented as mean  $\pm$  standard deviation ( $n=6$ ). Significant differences (\*\*\* $p<0.001$ ) are performed by Student's *t*-test. **g** Immunohistochemical staining of GPX4 and SLC7A11 in tumor section arrays. Scale bar: 20  $\mu$ m.

that the expression of GPX4 and SLC7A11 [6] in the erastin-treated group was decreased compared with the control group, which further verified the occurrence of ferroptosis within the tumor (Fig. 6g). In addition, the presence of GABA in protein hydrolysates might be a measure of hydroxyl radicals-mediated pro-containing peptides degradation [38]. When erastin-induced ferroptosis occurred, DR-1 was injected intravenously. Subsequently, GABA was detected and its concentration peaked at 1 h (Figure S15). Therefore, the *in vivo* fluorescence imaging results also confirmed that DR-1 was suitable for the detection of ferroptosis in living animals.

## Conclusion

In summary, DR-1 was designed and synthesized as a dual-response turn-on fluorescence probe for simultaneous Fe(II) and ROS detection during ferroptosis. During ferroptotic cell death, the upregulation of ROS levels led to the cleavage of the quenching group of DR-1, and the aggregation of Fe(II) resulted in fluorescence recovery. The fluorescence imaging results *in vitro* and *in vivo* showed that the fluorescence of DR-1 could be turned on sharply by the occurrence of ferroptosis. Using DR-1, we confirmed that ferroptosis was accompanied by noticeable ROS and Fe(II) generation. Owing to its good biocompatibility and simple synthesis, DR-1 may be useful for the detection of ferroptosis in a wide variety of cells and tissues. The distinctive features of DR-1 make this fluorescent probe suitable for investigating the ferroptosis process in real time and screening agents that either inhibit or induce ferroptosis.

**Supplementary Information** The online version contains supplementary material available at <https://doi.org/10.1007/s11307-022-01774-6>.

**Acknowledgements** The authors would like to acknowledge the instrumental technical support of the Multimodal Biomedical Imaging Experimental Platform, Institute of Automation, Chinese Academy of Sciences.

The authors would also like to thank Dr. Fudi Wang (Zhejiang University School of Medicine, China) for his critical review of the manuscript.

**Funding** This work was supported in part by the National Key Research and Development Program of China under Grants 2017YFA0700401, 2016YFC0103803, and 2017YFA0205200, National Natural Science Foundation of China (grants nos. 62027901, 81227901, 81930053, 81827808, 81527805, 81971198, and 81671851), China Postdoctoral Science Foundation (grant nos. 2020M680301 and 2019TQ0018), Chinese Academy of Sciences Youth Innovation Promotion Association (grant no. 2018167), Chinese Academy of Sciences Key Technology Talent Program, and Project of High-Level Talents Team Introduction in Zhuhai City (Zhuhai HLHPTP201703), The Fundamental Research Funds for the Central Universities (grant no. JKF-YG-22-B005).

## Declarations

**Conflict of Interest** The authors declare no competing interests.

## References

- Dixon SJ, Lemberg KM, Lamprecht MR, Skouta R, Zaitsev EM, Gleason CE, Patel DN, Bauer AJ, Cantley AM, Yang WS, Morrison B, Stockwell BR (2012) Ferroptosis: an iron-dependent form of nonapoptotic cell death. *Cell* 149(5):1060–1072
- Gaschler MM, Andia AA, Liu HR, Csuka JM, Hurlocker B, Vaiana CA, Heindel DW, Zuckerman DS, Bos PH, Reznik E, Ye LF, Tyurina YY, Lin AJ, Shchepinov MS, Chan AY, Peguero-Pereira E, Fomich MA, Daniels JD, Bekish AV, Shmanai VV, Kagan VE, Mahal LK, Woerpel KA, Stockwell BR (2018) FINO2 initiates ferroptosis through GPX4 inactivation and iron oxidation. *Nat Chem Biol* 14(5):507
- Yang WS, SriRamaratnam R, Welsch ME, Shimada K, Skouta R, Viswanathan VS, Cheah JH, Clemons PA, Shamji AF, Clish CB, Brown LM, Girotti AW, Cornish VW, Schreiber SL, Stockwell BR (2014) regulation of ferroptotic cancer cell death by GPX4. *Cell* 156(1–2):317–331
- Hangauer MJ, Viswanathan VS, Ryan MJ, Bole D, Eaton JK, Matov A, Galeas J, Dhruv HD, Berens ME, Schreiber SL, McCormick F, McManus MT (2017) Drug-tolerant persister cancer cells are vulnerable to GPX4 inhibition. *Nature* 551(7679):247–250
- Ursini F, Maiorino M (2020) Lipid peroxidation and ferroptosis: the role of GSH and GPx4. *Free Radic Biol Med* 152:175–185
- Jiang L, Kon N, Li TY, Wang SJ, Su T, Hibshoosh H, Baer R, Gu W (2015) Ferroptosis as a p53-mediated activity during tumour suppression. *Nature* 520(7545):57
- Viswanathan VS, Ryan MJ, Dhruv HD, Gill S, Eichhoff OM, Seashore-Ludlow B, Kaffenberger SD, Eaton JK, Shimada K, Aguirre AJ, Viswanathan SR, Chattopadhyay S, Tamayo P, Yang WS, Rees MG, Chen SX, Boskovic ZV, Javaid S, Huang C, Wu XY, Tseng YY, Roider EM, Gao D, Cleary JM, Wolpin BM, Mesirov JP, Haber DA, Engelman JA, Boehm JS, Kotz JD, Hon CS, Chen Y, Hahn WC, Levesque MP, Doench JG, Berens ME, Shamji AF, Clemons PA, Stockwell BR, Schreiber SL (2017) Dependency of a therapy-resistant state of cancer cells on a lipid peroxidase pathway. *Nature* 547(7664):453
- Yu YY, Jiang L, Wang H, Shen Z, Cheng Q, Zhang P, Wang JM, Wu Q, Fang XX, Duan LY, Wang SF, Wang K, An P, Shao T, Chung RT, Zheng SS, Min JX, Wang FD (2020) Hepatic transferrin plays a role in systemic iron homeostasis and liver ferroptosis. *Blood* 136(6):726–739
- Stockwell BR, Angeli JPF, Bayir H, Bush AI, Conrad M, Dixon SJ, Fulda S, Gascon S, Hatzios SK, Kagan VE, Noel K, Jiang XJ, Linkermann A, Murphy ME, Overholtzer M, Oyagi A, Pagnussat GC, Park J, Ran Q, Rosenfeld CS, Salnikow K, Tang DL, Torti FM, Torti SV, Toyokuni S, Woerpel KA, Zhang DD (2017) Ferroptosis: a regulated cell death nexus linking metabolism. *Redox Biology, and Disease, Cell* 171(2):273–285
- Liang C, Zhang XL, Yang MS, Dong XC (2019) Recent progress in ferroptosis inducers for cancer therapy. *Adv Mater* 31(51)
- Chen Y, Liu Y, Lan T, Qin W, Zhu YT, Qin K, Gao JJ, Wang HB, Hou XM, Chen N, Angeli JPF, Conrad M, Wang C (2018) Quantitative profiling of protein carbonylations in ferroptosis by an aniline-derived probe. *J Am Chem Soc* 140(13):4712–4720
- Wang KN, Liu LY, Mao D, Xu SD, Tan CP, Cao Q, Mao ZW, Liu B (2021) A polarity-sensitive ratiometric fluorescence probe for monitoring changes in lipid droplets and nucleus during ferroptosis. *Angew Chem Int Edit* 60(27):15095–15100
- Li HY, Shi W, Li XH, Hu YM, Fang Y, Ma HM (2019) Ferroptosis accompanied by (OH)-O-center dot generation and cytoplasmic viscosity increase revealed via dual-functional fluorescence probe. *J Am Chem Soc* 141(45):18301–18307



14. Gao MH, Monian P, Quadri N, Ramasamy R, Jiang XJ (2015) Glutaminolysis and transferrin regulate ferroptosis. *Mol Cell* 59(2):298–308
15. Imai H, Matsuoka M, Kumagai T, Sakamoto T, Koumura T (2017) Lipid peroxidation-dependent cell death regulated by GPx4 and ferroptosis. *Curr Top Microbiol* 403:143–170
16. Sies H, Jones DP (2020) Reactive oxygen species (ROS) as pleiotropic physiological signalling agents. *Nat Rev Mol Cell Bio* 21(7):363–383
17. Takashi Y, Tomita K, Kuwahara Y, Roudkenar MH, Roushdeh AM, Igarashi K, Nagasawa T, Nishitani Y, Sato T (2020) Mitochondrial dysfunction promotes aquaporin expression that controls hydrogen peroxide permeability and ferroptosis. *Free Radic Biol Med* 161:60–70
18. Li H, Shi W, Li X, Hu Y, Fang Y, Ma H (2019) Ferroptosis accompanied by (\*OH) generation and cytoplasmic viscosity increase revealed via dual-functional fluorescence probe. *J Am Chem Soc* 141(45):18301–18307
19. Hou W, Xie YC, Song XX, Sun XF, Lotze MT, Zeh HJ, Kang R, Tang DL (2016) Autophagy promotes ferroptosis by degradation of ferritin. *Autophagy* 12(8):1425–1428
20. Chen X, Yu CH, Kang R, Kroemer G, Tang DL (2021) Cellular degradation systems in ferroptosis. *Cell Death Differ* 28(4):1135–1148
21. Angeli JPF, Schneider M, Proneth B, Tyurina YY, Tyurin VA, Hammond VJ, Herbach N, Aichler M, Walch A, Eggenhofer E, Basavara-jappa D, Radmark O, Kobayashi S, Seibt T, Beck H, Neff F, Esposito I, Wanke R, Forster H, Yefremova O, Heinrichmeyer M, Bornkamm GW, Geissler EK, Thomas SB, Stockwell BR, O'Donnell VB, Kagan VE, Schick JA, Conrad M (2014) Inactivation of the ferroptosis regulator Gpx4 triggers acute renal failure in mice. *Nat Cell Biol* 16(12):1180–U120
22. Wang YQ, Chang SY, Wu Q, Gou YJ, Jia LP, Cui YM, Yu P, Shi ZH, Wu WS, Gao GF, Chang YZ (2017) The protective role of mitochondrial ferritin on erastin-induced ferroptosis. *Am J Hematol* 92(8):E459–E459
23. Toyokuni S, Yanatori I, Kong YY, Zheng H, Motooka Y, Jiang L (2020) Ferroptosis at the crossroads of infection, aging and cancer. *Cancer Sci* 111(8):2665–2671
24. Hirayama T (2019) Fluorescent probes for the detection of catalytic Fe(II) ion. *Free Radical Bio Med* 133:38–45
25. Dikalov SI, Harrison DG (2014) Methods for detection of mitochondrial and cellular reactive oxygen species. *Antioxid Redox Sign* 20(2):372–382
26. Aron AT, Loehr MO, Bogen J, Chang CJ (2016) An endoperoxide reactivity-based FRET probe for ratiometric fluorescence imaging of labile iron pools in living cells. *J Am Chem Soc* 138(43):14338–14346
27. Zhou J, Ma HM (2016) Design principles of spectroscopic probes for biological applications (vol 7, pg 6309, 2016). *Chem Sci* 7(10):6575–6575
28. Miao QQ, Yeo DC, Wiraja C, Zhang JJ, Ning XY, Xu CJ, Pu KY (2018) Near-infrared fluorescent molecular probe for sensitive imaging of keloid. *Angew Chem Int Edit* 57(5):1256–1260
29. Wang M-Y, Yuan A, Zhang J, Xiang Y, Yuan Z (2020) Functional near-infrared spectroscopy can detect low-frequency hemodynamic oscillations in the prefrontal cortex during steady-state visual evoked potential-inducing periodic facial expression stimuli presentation. *Vis Comput Ind Biomed Art* 3(1):28. <https://doi.org/10.1186/s42492-020-00065-7>
30. Hirayama T, Okuda K, Nagasawa H (2013) A highly selective turn-on fluorescent probe for iron(II) to visualize labile iron in living cells. *Chem Sci* 4(3):1250–1256
31. Mai TT, Hamai A, Hienzscha C, Caneque T, Muller S, Wicinski J, Cabaud O, Leroy C, David A, Acevedo V, Ryo A, Ginestier C, Birnbaum D, Charafe-Jauffret E, Codogno P, Mehrpour M, Rodriguez R (2017) Salinomycin kills cancer stem cells by sequestering iron in lysosomes. *Nat Chem* 9(10):1025–1033
32. Liang C, Zhang X, Yang M, Dong X (2019) Recent progress in ferroptosis inducers for cancer therapy. *Adv Mater* 31(51):e1904197
33. Aron AT, Reeves AG, Chang CJ (2018) Activity-based sensing fluorescent probes for iron in biological systems. *Curr Opin Chem Biol* 43:113–118
34. Hirayama T, Tsuboi H, Niwa M, Miki A, Kadota S, Ikeshita Y, Okuda K, Nagasawa H (2017) A universal fluorogenic switch for Fe(II) ion based on N-oxide chemistry permits the visualization of intracellular redox equilibrium shift towards labile iron in hypoxic tumor cells. *Chem Sci* 8(7):4858–4866
35. Wang Y, Li C, Zhang X, Kang X, Li Y, Zhang W, Chen Y, Liu Y, Wang W, Ge M, Du L (2021) Exposure to PM2.5 aggravates Parkinson's disease via inhibition of autophagy and mitophagy pathway. *Toxicology* 456:152770
36. Gupta MK, Lee SH, Crowder SW, Wang X, Hofmeister LH, Nelson CE, Bellan LM, Duvall CL, Sung HJ (2015) Oligoproline-derived nanocarrier for dual stimuli-responsive gene delivery. *J Mater Chem B* 3(36):7271–7280
37. Kawasaki R, Tsuchiya K, Kodama Y, Numata K (2020) Development of reactive oxygen species-triggered degradable nanoparticles using oligoproline-containing peptides. *Biomacromol* 21(10):4116–4122
38. Stadtman ER, Levine RL (2003) Free radical-mediated oxidation of free amino acids and amino acid residues in proteins. *Amino Acids* 25(3–4):207–218
39. Mandal S, Mann G, Satish G, Briki A (2021) Enhanced live-cell delivery of synthetic proteins assisted by cell-penetrating peptides fused to DABCYL. *Angew Chem Int Ed Engl* 60(13):7333–7343
40. Duelli DM, Lazebnik YA (2000) Primary cells suppress oncogene-dependent apoptosis. *Nat Cell Biol* 2(11):859–862
41. Manz DH, Blanchette NL, Paul BT, Torti FM, Torti SV (2016) Iron and cancer: recent insights. *Ann NY Acad Sci* 1368:149–161
42. Tian RL, Abarientos A, Hong JS, Hashemi SH, Yan R, Drager N, Leng K, Nalls MA, Singleton AB, Xu K, Faghri F, Kampmann M (2021) Genome-wide CRISPRi/a screens in human neurons link lysosomal failure to ferroptosis. *Nat Neurosci* 24(7):1020–1034
43. Hirayama T, Miki A, Nagasawa H (2019) Organelle-specific analysis of labile Fe(II) during ferroptosis by using a cocktail of various colour organelle-targeted fluorescent probes. *Metallomics* 11(1):111–117
44. Hirayama T, Inden M, Tsuboi H, Niwa M, Uchida Y, Naka Y, Hozumi I, Nagasawa H (2019) A Golgi-targeting fluorescent probe for labile Fe(II) to reveal an abnormal cellular iron distribution induced by dysfunction of VPS35. *Chem Sci* 10(5):1514–1521
45. Roverato ND, Sailer C, Catone N, Aichele A, Stengel F, Groettrup M (2021) Parkin is an E3 ligase for the ubiquitin-like modifier FAT10, which inhibits Parkin activation and mitophagy. *Cell Rep* 34(11):108857
46. Yao J, Cheng Y, Zhou M, Zhao S, Lin S, Wang X, Wu J, Li S, Wei H (2018) ROS scavenging Mn3O4 nanozymes for in vivo anti-inflammation. *Chem Sci* 9(11):2927–2933

**Publisher's Note** Springer Nature remains neutral with regard to jurisdictional claims in published maps and institutional affiliations.

Springer Nature or its licensor holds exclusive rights to this article under a publishing agreement with the author(s) or other rightsholder(s); author self-archiving of the accepted manuscript version of this article is solely governed by the terms of such publishing agreement and applicable law.